Fatigue of 316L stainless steel notched

Ferdinando Auricchio, Andrei Constantinescu, Giulia Scalet

Fatigue of 316L stainless steel notched μm-size components

F. Auricchio [a], A. Constantinescu [b], G. Scalet [a,*]

[a] *Dipartimento di Ingegneria Civile e Architettura, Università di Pavia, Via Ferrata 3, 27100 Pavia, Italy*
[b] *Laboratoire de Mécanique des Solides - CNRS UMR 7649, École Polytechnique, 91128 Palaiseau cedex, France*

The aim of the present paper is to provide an in-depth analysis of the fatigue-life assessment for μm-size 316L stainless steel components. Such components find typical applications in the biomedical field, e.g., in cardiovascular stents. To this purpose, the present work analyzes experimental data on 316L stainless steel from literature for smooth and notched μm-size components using a global computational approach. Several aspects are discussed: (i) the choice of an appropriate constitutive law for cyclic material behavior, (ii) fatigue criteria based on shakedown concepts for finite and infinite lifetime, in par-ticular distinguishing between low, high and very high-cycle fatigue regimes (denoted as LCF, HCF and VHCF, respectively), and (iii) gradient effects in relation with hot-spot as well as average or mean volume approaches for the lifetime estimation. The results give a new insight into the lifetime design of μm-size components and could be directly applied for the fatigue-life assessment of small size structures as, for instance, cardiovascular 316L stainless steel stents.

1. Introduction

In the past fifty years, austenitic stainless steels have been widely and extensively used in several fields, ranging from nuclear or aerospace industries to chemistry or food and beverage processing [1]. In particular, type 316L stainless steel has been largely appreciated for its high ductility and strength under complex thermomechanical loadings, i.e., such a material can reach considerable plastic strains of 0.5–1% at millions of cycles. However, materials like the 316L or 304L stainless steels present a complex material behavior characterized by primal and secondary hardening [2–5], which make the design of structures a difficult task. Nowadays, in spite of a large database of models and experimental data [6], both experimental [7–9] and modeling campaigns [10–14] are still continuing in order to improve both safety and performance of the designed structures.

In the recent decades, type 316L stainless steel has gained a privileged position among the materials employed in biomedical devices, e.g., stents, vena cava filters, guide-wires for catheters and pacemaker leads [15,16]. The attractive properties of such a material, e.g., well adapted mechanical characteristics (great ductility, high tensile strength, and a raised elastic limit), biocompatibility, resistance to corrosion as well as fatigue performances, assure the long-term service required by biomedical devices. However, the biomedical field is imposing two specific constraints in the design of 316L stainless steel devices: (i) the interest in the VHCF domain (i.e., 10^7–10^8 cycles) and (ii) the use of mm- and μm-size components.

As an example, cardiovascular 316L stainless steel stents have to withstand both their initial deployment within the artery, which involves large amounts of plastic deformation, and the long-term service loading induced by the pulsing blood pressure [17]. In particular, such devices must withstand at least 10 years service without failure [18]. Such a constraint translates into 400 million (i.e., 4×10^8) cycles during stent lifetime, since 70 artery pulses per minute impose 40 million cycles per year.

Moreover, stents are manufactured either through welding of microscopic wires or through laser cutting from thin-walled tubes, both leading to a final truss-type structure composed of struts connected by hinges, with thicknesses in the range of 50–150 μm [19–22]. Stents manufactured through both processes will finally present small radius and thus will be subjected to stress concentrations [23]. Also, μm-size components like stents have length scale in the order of magnitude of the length of grains characterizing their microstructure, i.e., the ratio between the length scales of the mesoscopic structure of grains and of the macroscopic structure of the device, characterized by approximately 10–20 grains across the section, makes the application of standard bulk models inadequate [19–22,24].

Additionally, in spite of the importance of such applications, insufficient (only few) data sets are available in the literature

* Corresponding author. Tel.: +39 0382 985468.
E-mail address: giulia.scalet@unipv.it (G. Scalet).

[23,25,26], due to practical difficulties of testing very small specimens. Standard mechanical test equipment is in fact not suitable for testing micrometric components due to the operating range and resolution of load and displacement transducers and the design of gripping members.

Thus, the design for reliability of cardiovascular stents is very complex, since it has to take into account HCF or VHCF loading, material and device specificities, manufacturing-induced features as well as corrosive environment.

In order to bridge the gap between the existing experiments and the fatigue design of such components, several numerically-based attempts have recently been proposed to assess the lifetime of these microscopic structures (see, e.g., [27–32]). Numerical simulations minimize the number of design cycles and structural experiments and prevent failure. However, the use of an appropriate constitutive law and the application of standard fatigue prediction criteria to biomedical devices have to be carefully investigated, since they could potentially produce non-conservative estimates of safe working loads in case of size effects and stress gradients, and thus they could result in vivo fractures of devices. Moreover, most of the available numerical approaches for the fatigue-life assessment of stents do not dispose of adequate criteria, i.e., identified on appropriate experimental data in terms of size and notch effects.

Accordingly, the aim of the present paper is to provide an in-depth analysis of the fatigue-life assessment of μm-size components for the design of stents manufactured by laser cutting. This is realized by revisiting the shakedown concepts and by taking into account several aspects characterizing stents, as the complex material behavior, size effects, and stress concentration features.

The practical difficulties of testing μm-size specimens and the inadequacy of fatigue data related to macroscopic specimens lead us to critically investigate and analyze two experimental campaigns available from the literature by Wiersma et al. [23,25] and Donnelly [26], on 316L stainless steel microscopic smooth and notched components, produced with the standard procedure applied in the stent manufacturing industry.

We complete the reported data by using a **global computational approach** consisting of the following two steps [33]:

i. a *mechanical analysis* to calculate the shakedown or stabilized mechanical state;
ii. a *fatigue analysis* to compute the number of cycles before failure. In particular, in case of elastic shakedown, we focus on the fatigue criterion by Dang Van [34] and, in case of plastic shakedown, on fatigue crack initiation criteria associated with hot-spot as well as mean or volume element approaches, i.e., the Manson–Coffin criterion [35,36], the dissipated energy per cycle criterion [37,38], and a modified version of the dissipated energy criterion [10–12].

The discussion of the shakedown state, resulting from the elasto-plastic mechanical analysis, allows to investigate several fatigue criteria for infinite and finite lifetime, in particular distinguishing between HCF, VHCF, and LCF regimes. We calibrate such criteria on the cited experimental data and therefore, we are able to provide a set of criteria that can be used to numerically predict the fatigue-life of cardiovascular 316L stainless steel stents. The obtained results assess the suitability of standard prediction methods, normally used for macroscopic components, for μm-size components and give a new insight into the treatment of fatigue issues in μm-size components.

Let us remark that the present approach is based on a purely macroscopic continuum material model, which has been largely applied to stents by continuum mechanics based methodologies as in, e.g., [27,28,31]. The approach based on macroscopic continuum models is a robust method but should be considered as a first approximation of the phenomena under investigation, since it is not appropriate to explicitly capture microstructural effects on neither grain plastic deformation nor the lifetime, which become significant when the length scale of the device dimensions is comparable with the one of the microstructure (e.g., grain size), as in cardiovascular stents. Stent struts typically have only a few grains across their thickness and stent performance may depend on the inhomogeneous microstructure which causes localized (grain level) plastic deformation even at macroscopically elastic strains [30].

Despite these remarks, most of the works on fatigue of stents ignore the inhomogeneous nature of the microstructure; see, e.g., [27,28,31].

In this context, crystal plasticity theory should be applied to model crack initiation and microstructurally small crack growth. Monotonic behavior of stent struts using crystal plasticity has been developed, for example, in [39,19,40,20]. Among the others, McGarry et al. [29] calibrated a crystal plasticity model for monotonic behavior and carried out a simple Goodman analysis. Recently, analyses based on polycrystalline computations for HCF predictions have been proposed in [41–44]. A number of microstructure-sensitive fatigue indicator parameters (FIPs), such as the accumulated crystallographic slip, used in conjunction with crystal plasticity theory, have successfully predicted fatigue crack initiation observed experimentally [45]. In the case of polycrystal ferritic steels, the recent work by Sweeney et al. [46] fully investigates fatigue crack nucleation combining experimental observations with microstructural representations of the same samples and using crystal plasticity finite element techniques. The results assess FIPs, together with the roles of elastic anisotropy and length scale effects in slip development, and hence in crack nucleation. In the context of fatigue performance of stents, Sweeney et al. [30] presented a finite element stent fatigue methodology based on crystal plasticity theory for the prediction of crack initiation, using microstructural FIPs. The methodology encompasses several aspects of micromechanical modeling, including realistic microstructure geometries, an appropriate crystal plasticity constitutive model as well as microstructure sensitive FIPs, based on accumulated plastic slip and strain energy dissipation. Similarly, the interesting work by Sweeney et al. [47] presents the development of a micromechanical framework for fatigue design, based on the experimental characterization of a biomedical CoCr alloy. The work presents the calibration of FIPs within the micromechanical framework for the prediction of microstructure-sensitive fatigue crack initiation and compares the predictions of fatigue crack initiation with traditional Basquin-Goodman total-life predictions, revealing more realistic scatter of data for the microstructure-based FIP approach.

The analysis of the experiments by Wiersma et al. [23,25] and Donnelly [26] using a crystal plasticity based approach and an appropriate fatigue criterion is a perspective of this work and will not be considered here.

The present paper is organized as follows. Section 2 revisits the two experimental campaigns. Then, Sections 3 and 4 present the performed mechanical and fatigue analyses. Conclusions and summary are finally given in Section 5.

2. 316L steel: material and fatigue data

The present work focuses on 316L austenitic stainless steel with chemical composition and thermo-mechanical properties given in Tables 1 and 2, see [48] for details.

Before entering into the details of the global computational approach adopted in the present work, this Section describes the

Table 1
Chemical composition (wt%) of 316L austenitic stainless steel [48].

Element	C	Mn	Si	S	P	Ni	Cr	Mo	Cu	N
Mass content (%)	0.024	1.86	0.36	0.0045	0.026	11.6	17.2	2.55	–	–

Table 2
Thermo-mechanical properties of 316L austenitic stainless steel [48].

T	°C	20	50	100	150	200	250	300	350
ν	–	0.3	0.3	0.3	0.3	0.3	0.3	0.3	0.3
E	10^3 MPa	197	195	191.5	187.5	184	180	176.5	172
α	10^{-6}/°C	15.54	16.0	16.49	16.98	17.47	17.97	18.46	18.95
$\frac{\lambda}{\rho C}$	10^{-6} m^2 s^{-1}	3.89	3.89	3.89	3.94	3.99	4.06	4.17	4.26
λ	W/m °C	14.0	15.2	15.4	15.8	16.6	17.3	17.9	18.6

main results of the two extensive experimental campaigns conducted on 316L specimens of micrometric size by Wiersma et al. [23,25] and Donnelly [26].

2.1. Experimental tests by Wiersma et al.

Wiersma et al. [23,25] carried out a complete experimental campaign on 316L stainless steel specimens taking the form of smooth and notched round/rectangular bars (see Fig. 1(a)–(d) and Tables 3 and 4). Specimens were produced with the standard procedure applied in the stent manufacturing industry: (i) laser cutting; (ii) vacuum anneal treatment or not; and (iii) electro-polishing. The size of the tested specimens was approximately 0.1 mm, thus comparable to that characterizing industrially produced stents. Moreover, the cross-section of the tested specimens contained around 10 grains.

Monotonic tensile test results are represented in terms of stress–strain curves in Fig. 2(a) and mechanical properties are reported in Table 5. The grain size and hardness values provided in Table 5 are identical for the macroscopic and microscopic specimens, confirming that the material itself is identical. The stress–strain curves show that μm-size annealed specimens, when compared to macroscopic specimens, display lower values of yield and ultimate tensile strengths and strain to failure, as well as larger

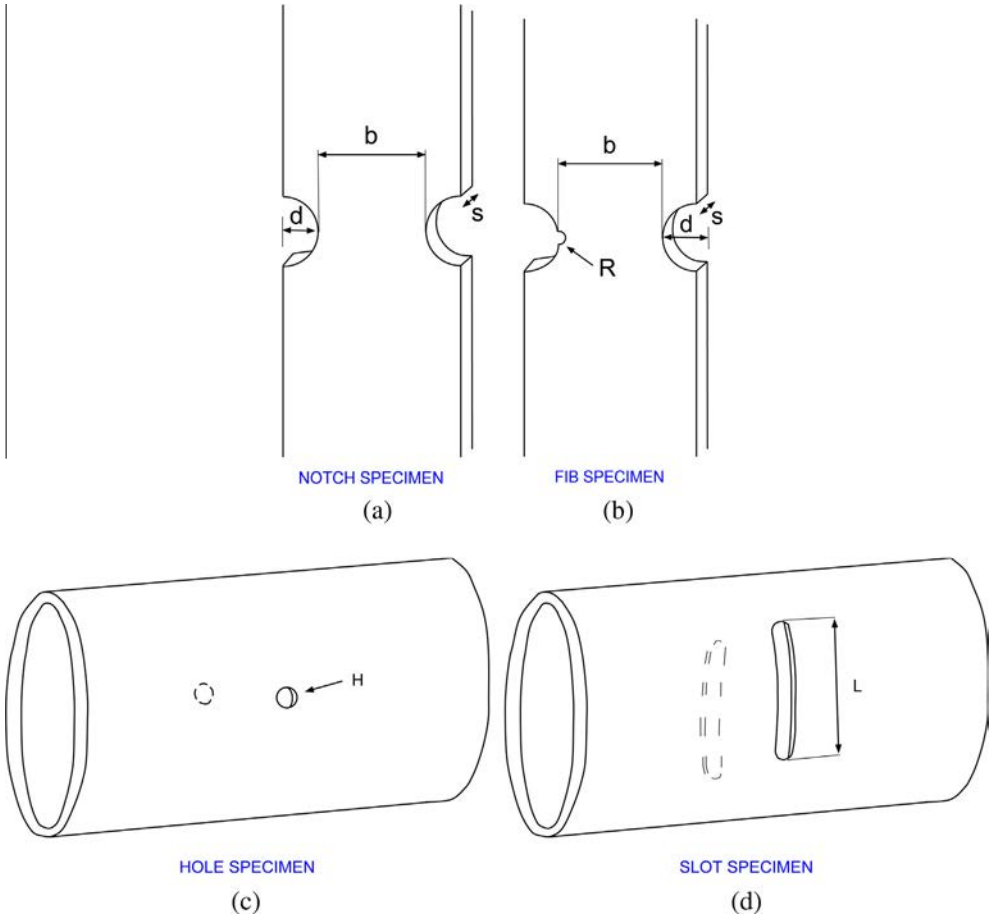

Fig. 1. Geometries of the 316L μm-size notched specimens tested by Wiersma et al. [23,25] (*b* is the net section; *s* the thickness; *d* the notch depth; *R* the fib-slot; *H* the hole radius; *L* the slot length).

Table 3
Summary of the tests on macroscopic 316L specimens and of the fatigue limits by Wiersma et al. [23,25].

Specimen	Features	Fatigue ratio (R)	Experimental fatigue limit (MPa)
MACRO			
Smooth	Round bar ($D = 7.5$ mm, gauge length 25 mm)	0.1	420
Notched	Round bar ($D = 12$ mm, circumf. V-shaped notch of depth 1 mm, root radius 0.08 mm)	0.1	150
		0.8	75

Table 4
Summary of the tests on μm-size 316L specimens and of the fatigue limits by Wiersma et al. [23,25].

Specimen	Features	Fatigue ratio (R)	Experimental fatigue limit (MPa)
MICRO			
Smooth	Rectangular bar (width 0.1 mm, thickness 0.09 mm)	0.1	420
50-notch	Rectangular bar (net section of 0.11 mm, thickness 0.09 mm, notch depth 0.05 mm)	0.1	360
100-notch	Rectangular bar (net section of 0.11 mm, thickness 0.09 mm, notch depth 0.1 mm)	0.1	355
145-notch	Rectangular bar (net section of 0.11 mm, thickness 0.09 mm, notch depth 0.145 mm)	0.1	350
50-fib	Rectangular bar (net section of 0.11 mm, thickness 0.09 mm, notch depth 0.05 mm, slot of 0.001 mm)	0.1	320
60-hole	Thin-walled tube (outer diameter 1.7 mm, wall thickness 0.09 mm, hole radius 0.06 mm)	0.1	250
400-slot	Thin-walled tube (outer diameter 1.7 mm, wall thickness 0.09 mm, slot length 0.4 mm)	0.1	120
1500-slot	Thin-walled tube (outer diameter 1.7 mm, wall thickness 0.09 mm, slot length 1.5 mm)	0.1	115

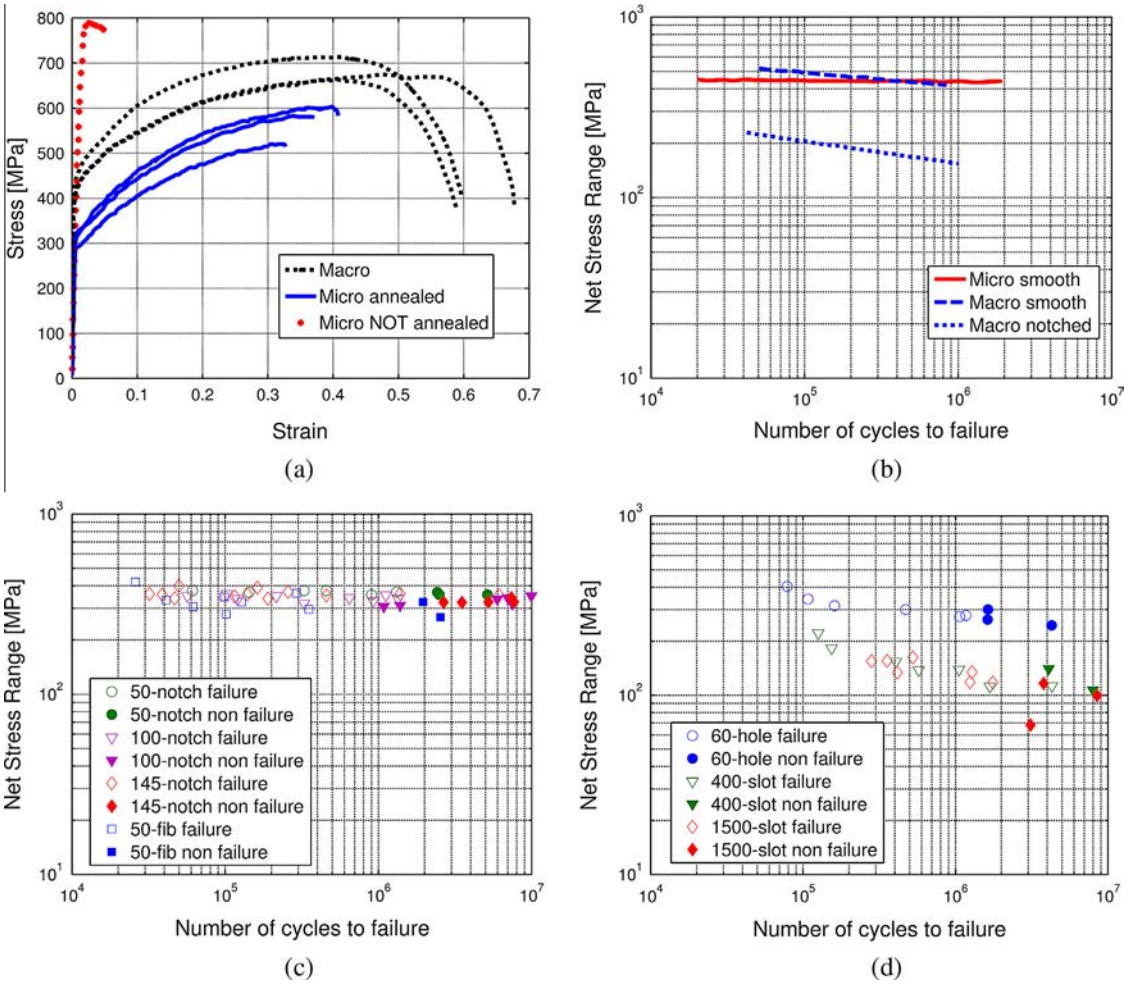

Fig. 2. Results from the experiments by Wiersma et al. [23,25]. (a) Stress vs. strain diagram from monotonic tensile tests. Net stress range vs. number of cycles to failure diagram from fatigue tensile tests on (b) smooth macroscopic and μm-size specimens; (c)–(d) notched μm-size specimens.

Table 5
Material properties from monotonic tensile tests by Wiersma et al. [23].

Specimen	Grain size (mm)	Yield strength (0.2% proof) (MPa)	Ultimate tensile strength (MPa)	Hardness (Vickers)	Strain to failure	Reduction in area (%)
MACRO	0.0115	396	754	186	0.60	73
MICRO	0.0105	315	580	170	0.37	87
MICRO (unannealed)	–	680	780	312	0.05	–

values of reduction in area before failure, thus demonstrating a size effect. Therefore, one can conclude that for annealed material decreasing specimen size reduces strength but increases ductility. On the contrary, unannealed specimens show a higher strength and lower ductility.

Fatigue tensile tests were carried out using a sinusoidal loading cycle with R ratios varying from 0.1 to 0.8 and are summarized in Tables 3 and 4. Fig. 2(b)–(d) shows fatigue tensile test results in terms of the applied stress range and the number of cycles to failure. The reported applied stress level for specimens with stress concentrations (notches or slots) is a mean stress level computed as the ratio between the applied force and the net area. Tables 3 and 4 summarize the obtained fatigue limits, defined as the values of the stress range for which the average number of cycles to failure is 2×10^6.

2.2. Experimental tests by Donnelly

Donnelly [26] carried out a complete experimental campaign on 316L stainless steel specimens taking the form of smooth rectangular bars (see Table 6). Again, specimens were produced with the standard procedure applied in the stent manufacturing industry: (i) laser cutting; (ii) vacuum anneal treatment; (iii) seamless tubing; and (iv) electro-polishing. The size of the tested specimens ranged from 0.05 to 0.15 mm, thus comparable to that characterizing industrially produced stents. The number of grains per cross-section ranged from 5 to 15.

Fatigue tensile tests were carried out using a push–pull traction cycle with R ratio of 0.5 and are summarized in Table 6. Fig. 3(a)–(b) shows the results of the monotonic and fatigue tensile tests, where the fatigue limit is defined as the value of the stress amplitude for which the average number of cycles to failure is 10^7. The fatigue limit decreases for the 50 μm specimen, which can be associated to a size effect.

3. 316L steel: constitutive law and mechanical analysis

In order to critically investigate the described experimental campaigns, this Section presents the first step of the adopted global computational approach, that is, a mechanical analysis to calculate the shakedown or stabilized mechanical state. In particular, we now describe first our modeling assumptions and the adopted constitutive law; then, we present the mechanical analysis performed with the finite element (FE) method. Models and analyses are realized using the object-oriented FE program, Cast3M (see, e.g., [49]).

3.1. Modeling assumptions

The cyclic behavior of 316L stainless steel shows exceptional ductility and a complex evolution which can be described by using a series of superposed hardening laws (see, e.g., [2–5]).

In the following, we adopt a simplifying view as proposed initially by Skelton [50,51] and successfully applied to LCF lifetime predictions in [10–12,33]. Such a view describes the cyclic material behavior, i.e., the recorded stress level under applied strain amplitude, and identifies three material behavior phases defined by the saturation, tangent, and final points, as shown in Fig. 4: (i) the hardening/softening phase [0-N_{sat}] corresponding to the stabilization of the plastic material properties; (ii) the stabilized phase [N_{sat}-N_{tan}] represented by a flat plateau with small property variations; and (iii) a final failure phase [$N_{tan} - N_{fin}$] characterized by a fast drop of the measured stress (as we impose the displacements/strains). Conventionally, N_{fin} is defined by a 5% or 10% load drop. During the saturation phase we assume that the structure has reached an asymptotic limit cyclic (plastic shakedown) which is described by the constitutive law and can be computed numerically on the structure under scrutinity.

Moreover, we reasonably admit that the mechanical response at $N_f = N_{fin}/2$ lies within the stabilized period and corresponds to material behavior identified for our computational needs (see Fig. 4). This is compatible with the fatigue analysis where characteristics used in the interpretation are equally taken after $N_{fin}/2$ cycles.

Such an approach neglects the fine description of real material behavior (see, e.g., [2–5]) and leads to an approximate error of about 5% in the computed stress level, which is of the order of magnitude of other uncertainties in the modeling. Similar assumptions have already been successfully used for thermo-mechanical fatigue predictions of 304L steel behavior [10–12] or other steels [50,51].

Recalling the discussion of Section 1, another modeling assumption concerns size effects and the application of a continuous model to a structure with sizes close to the grain size, along the line of the methodologies proposed in, e.g., [27,28,31]. We assume

Table 6
Summary of the tests on μm-size 316L specimens and of the fatigue limits by Donnelly [26].

Specimen	Features	Fatigue ratio (R)	Experimental fatigue limit (MPa)
MICRO			
Smooth 50 μm	Rectangular bar (width 0.05 mm, thickness 0.06 mm)	0.5	120
Smooth 75 μm	Rectangular bar (width 0.075 mm, thickness 0.06 mm)	0.5	150
Smooth 100 μm	Rectangular bar (width 0.1 mm, thickness 0.06 mm)	0.5	150
Smooth 150 μm	Rectangular bar (width 0.15 mm, thickness 0.06 mm)	0.5	150

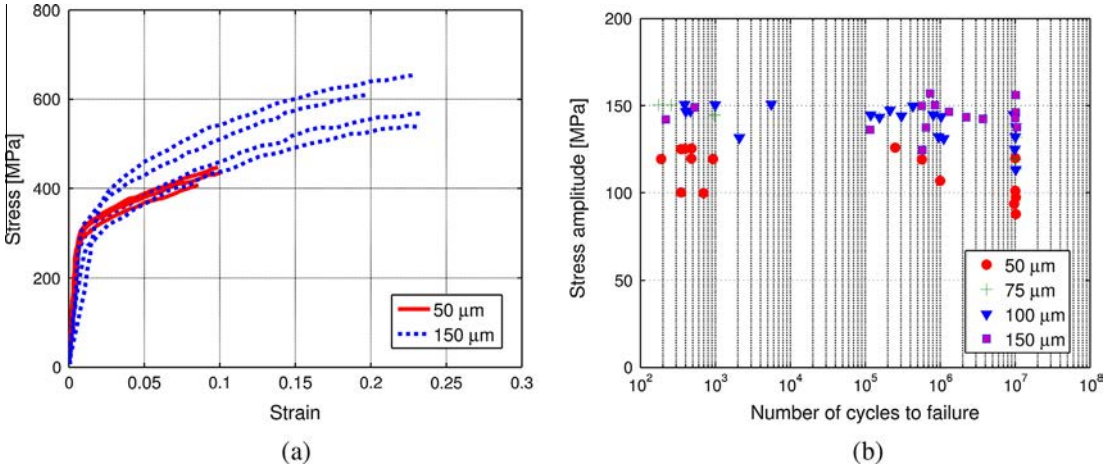

Fig. 3. Results from the experiments by Donnelly [26]. (a) Stress vs. strain diagram from monotonic tensile tests; (b) stress amplitude vs. number of cycles to failure from fatigue tensile tests on μm-size specimens.

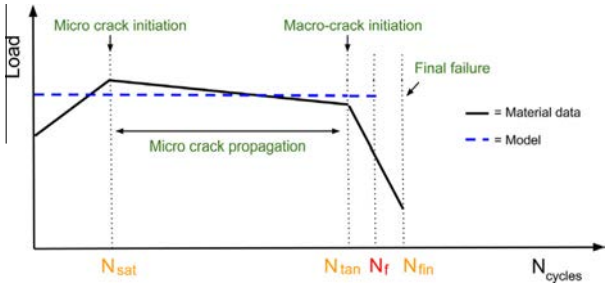

Fig. 4. Schematic representation of the cyclic material behavior adopted in the present approach (see also [50,51]).

that the present analysis will provide a typical 'mean' answer of the structure and that the inherent variability of the properties of the microstructure will provide the spread of the fatigue lifetime. However, such an aspect is not treated here and will be the object of future work.

Moreover, since an important feature of cardiovascular stent applications is given by their small size, where the size of the structure is close to that of the representative volume element, one could reasonably suggest that an appropriate model should include crystal plasticity, as treated in detail by [46,47,30]. However, this would further imply that the microstructure is precisely known, or that a Monte Carlo method need to be employed to estimate the solution for different grain orientations [52]. Here, we consider a homogenized macroscopic approach and we further assume that size effects are taken into account through the fatigue-life estimations based on μm-size experiments.

3.2. Adopted constitutive model for 316L stainless steel

The elasto-plastic constitutive model has a J2 yield function and non-linear isotropic and kinematic hardening (with one kinematic center) [6,53–55]. On the one side, isotropic hardening controls the rate at which the stabilized response is achieved, by allowing yield surface expansion and thus, by defining the evolution of stress magnitudes reached in a cyclic stress–strain response; on the other side, kinematic hardening influences the shape of the stabilized hysteresis curve, by allowing yield surface displacement and thus, by introducing a back stress into the cyclic stress–strain response, which reduces yield stress upon reversal of loading.

The multiaxial equation for the back stress tensor, $\mathbf{X}$, is defined by:

$$\dot{\mathbf{X}} = \frac{2}{3} C(p)\dot{\boldsymbol{\varepsilon}}^p - \gamma \mathbf{X}\dot{p} \tag{1}$$

with $C(p) = C_\infty(1 + (\psi - 1)\exp^{-\omega p})$ and $\dot{p} = \sqrt{2/3\ \dot{\boldsymbol{\varepsilon}}^p : \dot{\boldsymbol{\varepsilon}}^p}$, where $\boldsymbol{\varepsilon}^p$ is the plastic strain tensor, p is the accumulated plastic strain, and C_∞, ψ, γ, and ω are kinematic constants. The isotropic hardening function, $R = R(p)$, is given by the following relation:

$$\dot{R} = b(R_\infty - R)\dot{p} \tag{2}$$

where R_∞ is the saturated value of isotropic hardening and b the rate of decay for isotropic hardening. The yield surface, $f = f(\boldsymbol{\sigma}, \mathbf{X}, p)$, is defined by the classical function:

$$f = \sqrt{\frac{3}{2}(\mathbf{s} - \mathbf{X}) : (\mathbf{s} - \mathbf{X})} - R_0 - R \tag{3}$$

where $\mathbf{s}$ is the deviatoric tensor for stress and R_0 the initial yield stress. The evolution law for the plastic strain, $\boldsymbol{\varepsilon}^p$, takes the form:

$$\dot{\boldsymbol{\varepsilon}}^p = \frac{3}{2}\dot{\xi}\ \frac{\mathbf{s} - \mathbf{X}}{\sqrt{\frac{3}{2}(\mathbf{s} - \mathbf{X}) : (\mathbf{s} - \mathbf{X})}} \tag{4}$$

In the absence of direct cyclic measurements on the fatigue experiments [25,23,26], we identify model parameters on the experiments by Lê [48], consisting of uniaxial strain-controlled tests with variable amplitude loading on cylindrical specimens. In particular, five variable loading amplitudes have been applied in the following sequence: ±0.30%, ±0.75%, ±2.00%, ±0.75%, and ±0.30%. Table 7 presents the sequence of the applied variable loading amplitudes and the related number of loading cycles; see [48] for further details. Table 8 lists the adopted constitutive model parameters. Fig. 5 shows a comparison between the stabilized

Table 7
Sequence of the five applied variable loading amplitudes and related number of loading cycles for the uniaxial strain-controlled tests on cylindrical specimens, conducted by Lê [48] and used for model calibration.

Loading amplitude (%)	Number of loading cycles
±0.30	25
±0.75	25
±2.00	10
±0.75	40
±0.30	40

Table 8
Summary of the adopted model parameters for 316L stainless steel [48].

Parameter	Description	Value
E	Young Modulus	196,000 MPa
ν	Poisson ratio	0.3
R_0	Initial yield stress	211 MPa
R_∞	Saturated value of isotropic hardening	231 MPa
b	Decay rate for isotropic hardening	6.69
C_∞	Kinematic constant	67,050 MPa
γ	Kinematic constant	218
ψ	Kinematic constant	0.73
ω	Kinematic constant	0.91

hysteresis loops predicted by the model and the experimental curves, for the five applied strain amplitudes, as reported by [48]. The model successfully captures the experimental loops.

Fig. 6(a)–(b) present the monotonic and stabilized stress–strain curves generated by the model with parameters of Table 8. The order of magnitude of the numerical stresses and strains with respect to the experimental ones is illustrated in Fig. 6(a)–(b) through a comparison with the monotonic experimental curves obtained by Wiersma et al. [25,23] and Donnelly [26]. As it can be observed, the numerical monotonic and stabilized curves lie within the experimental stress range. However, large errors in terms of stresses (up to 30%) are particularly evident through

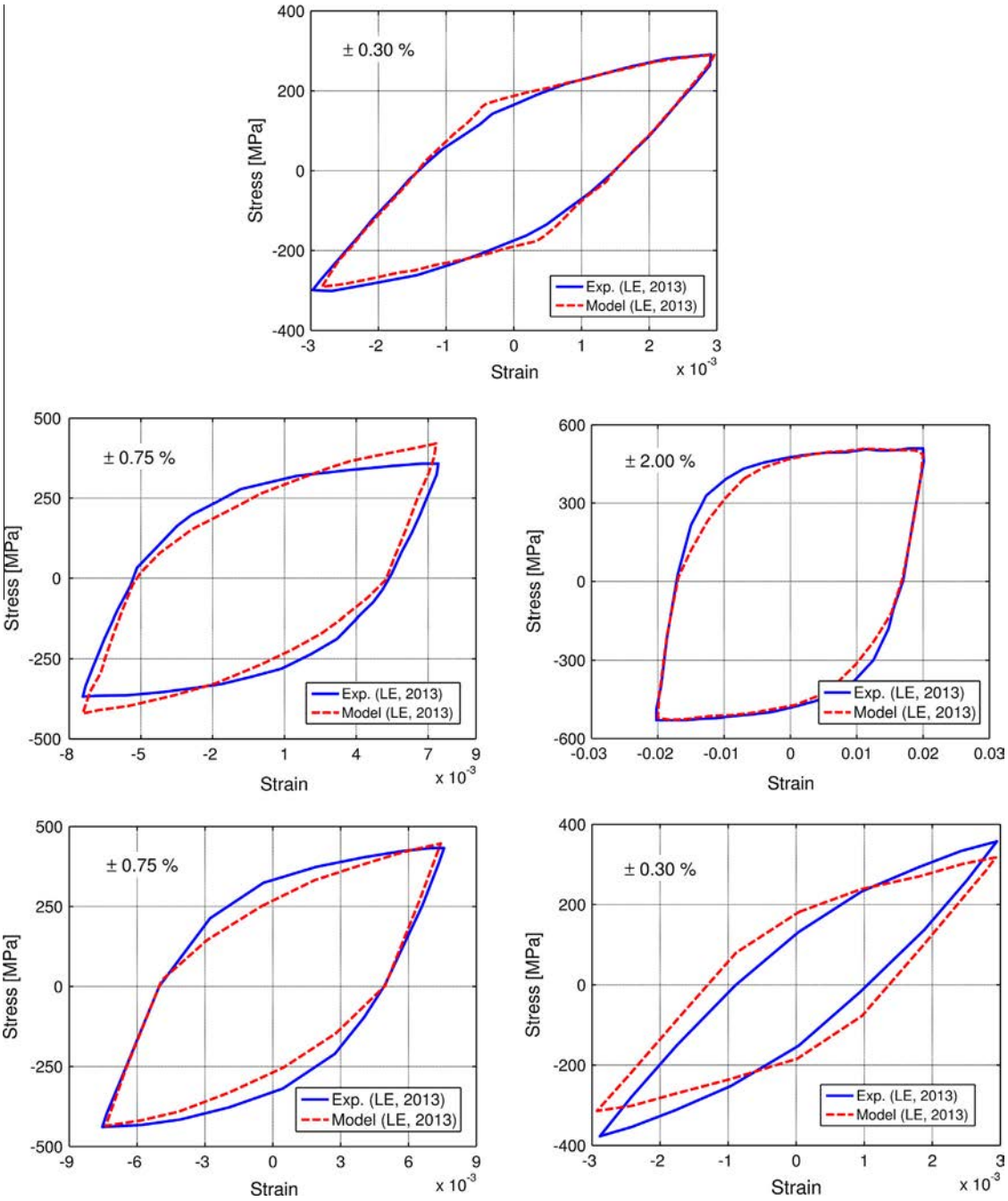

Fig. 5. Comparison between the stabilized hysteresis loops generated by the adopted model and the experimental data by Lê [48] for the five applied strain amplitudes listed in Table 7.

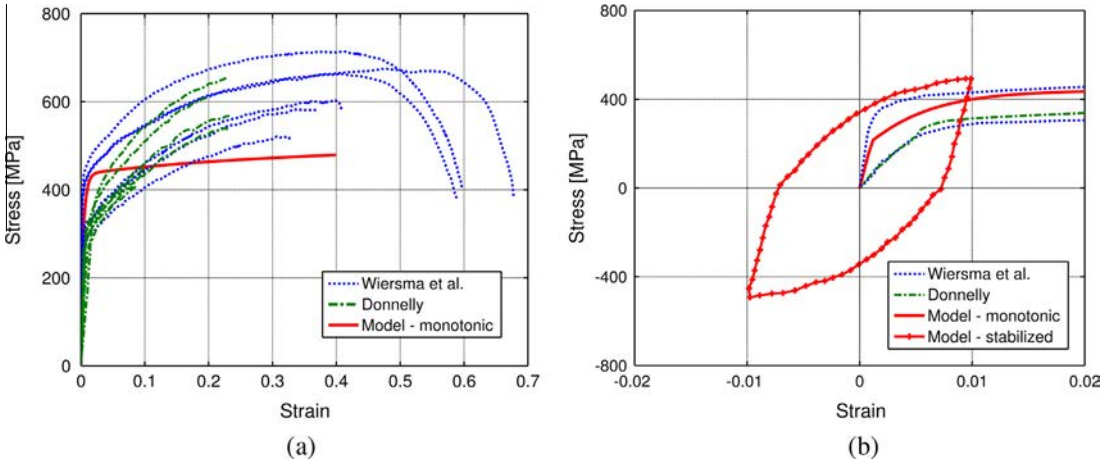

Fig. 6. (a) Comparison between monotonic stress–strain tensile curves obtained by the adopted model and by Wiersma et al. [25,23] and Donnelly [26]; and (b) stabilized hysteresis curve generated by the adopted model compared to monotonic tensile curves by Wiersma et al. [25,23] and Donnelly [26].

the comparison between monotonic curves. This is attributed to the fact that we adopt a model calibrated on experimental stabilized curves [48], due to the absence of direct cyclic measurements on the fatigue experiments by Wiersma et al. [25,23] and Donnelly [26]. However, the calibration of the constitutive models against both cyclic and tensile data is important in applications characterized by high initial plastic deformation, which induces high residual or mean stresses, followed by fatigue, such as for a stent where crimping, crimp recoil, deployment and recoil incur plastic deformation, followed by systolic-diastolic pulsatile loading [30,47]. In spite of the overall agreement between predictions and measurements, the preceding calibration of the constitutive law has been applied with precaution to μm-size structures. If the structures under scrutiny are, for example, stents, one should take into account (i) that their shape is close to that of wires and we can expect a modification of the exact parameter values as also the difference between the 50 and 150 μm specimens is about 20% (see Fig. 3) and (ii) that such structures are subjected to large plastic deformation before the fatigue cycling. The operations of crimping, crimp recoil, deployment and recoil, which incur plastic deformation, then followed by systolic-diastolic pulsatile loading [30,47], illustrate our point.

3.3. Mechanical analysis of experiments by Wiersma et al. and Donnelly

A complete series of elasto-plastic FE analyses is performed on each specimen in accordance to the loading cycle of experiments [26,25,23]. In the case of notched specimens, a preliminary analysis is accomplished in order to asses the accuracy of the solution at the notch tip. The mesh refinement is stopped when the elastic solution converges and, therefore, correctly represents the solution.

We consider the notched specimens of Fig. 1(a)-(d) and we generate all the meshes for the specimens taking the form of rectangular bars (i.e., the 50-notch, 100-notch, 145-notch, and 50-fib specimens) using two-dimensional 6-node quadratic plain stress elements, due to the lack of constraint in the thickness direction of these specimens. Then, we generate the meshes of the specimens taking the form of tubes (i.e., the 60-hole, 400-slot, and 1500-slot specimens) using three-dimensional 20-node quadratic brick elements.

According to the symmetry of the problem, we model only one quarter of each specimen, except for the 50-fib specimen for which we model only one half (see Fig. 7(a)–(d)). The finest zone of the mesh corresponds to the notched zone of the specimen and the elements in this part of the mesh are refined depending on the dimension of the notch radius and of the grain size. In particular, specimens are meshed using 4662 elements for the 50-notch, 6582 for the 100-notch, 9068 for the 145-notch, 75,000 for the 50-fib, 61,624 for the 60-hole, 23,346 for the 400-slot, and 25,473 for the 1500-slot (see Fig. 7(a)–(d)). Compared to the grain size, we assume approximately 5 elements per grain size. Consequently, the smallest element size at the root of the notch is characterized by an element size/notch radius ratio ranging between 0.0013 and 0.04. To estimate possible errors due to large spatial gradients, we test finer meshes and we can report that refining mesh above the present limit causes an important increase of computing time without a noticeable improvement of the results (see Section 3.4 for details).

3.4. Results and discussions

As a result of the conducted elasto-plastic FE analyses, we obtain elastic shakedown for the experiments on smooth specimens by Wiersma et al. [25,23] and Donnelly [26] and plastic shakedown for the experiments on notched specimens by Wiersma et al. [25,23].

In order to avoid possible material failures, we first compare the computed strains to the experimental strains to failure (see Table 5) and to the strains of the monotonic curves of Fig. 6(a)–(b). The computed strains lie in the range 0.01–0.1 for all the specimens and loading conditions, thus avoiding possible premature failures.

Fig. 8 shows the distribution of the dissipated energy, W^p, at the stabilized cycle, defined as follows:

$$W^p = \int_{cycle} \boldsymbol{\sigma} : \dot{\boldsymbol{\varepsilon}}^p dt \tag{5}$$

for the 50-notch specimen of Fig. 1(a), subjected to a net pressure range of 360 MPa (see Fig. 2(c)). As it can be observed, plasticity is localized in a very small region of about 0.01 mm (grain size) around the notch, where W^p assumes a maximum value of about 1 MPa; the remaining part of the specimen presents an elastic shakedown state and no W^p is manifested. The dissipated energy, W^p, is also plotted along the edge AB in Fig. 8. Moreover, Fig. 9 shows how mesh refinement does not allow noticeable improvements of the results in terms of dissipated energy.

The 100-notch and 145-notch specimens present similar results since they have the same net section.

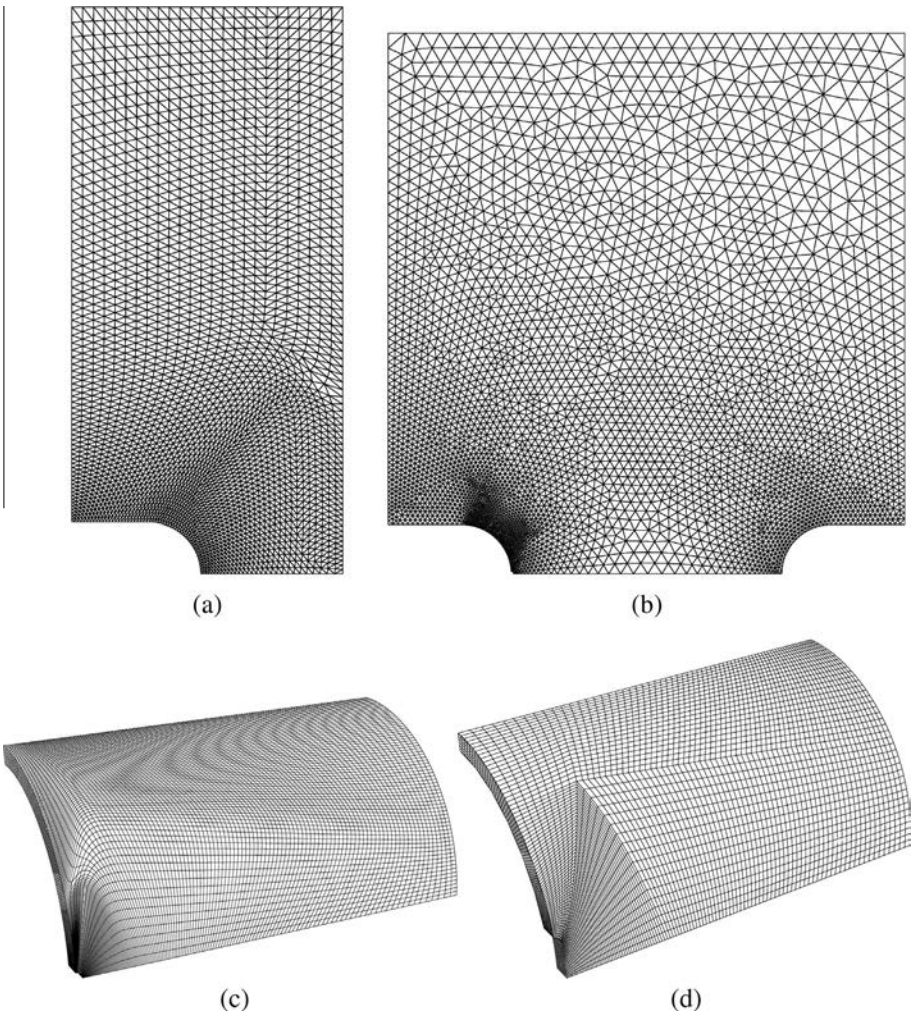

Fig. 7. Adopted meshes for the specimens of Fig. 1(a)–(d). 2D quadratic plain stress elements for the (a) notch and (b) fib specimens; 3D quadratic brick elements for the (c) hole and (d) slot specimens.

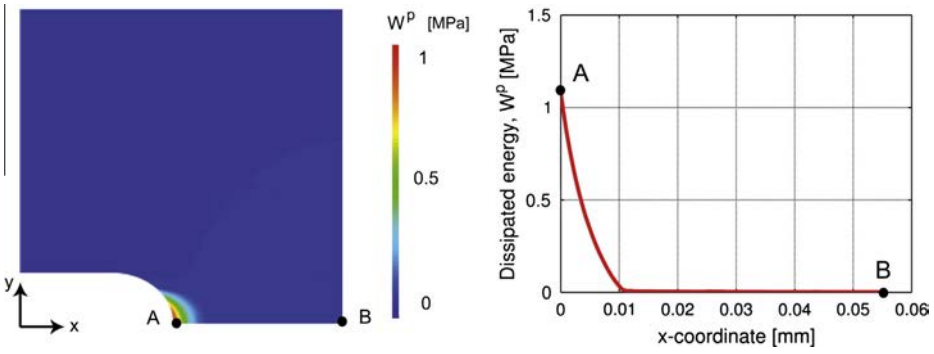

Fig. 8. Results of the mechanical analysis for the 50-notch specimen subjected to a net pressure range of 360 MPa. Distribution of the dissipated energy, W^p, in the specimen (left) and along the edge AB (right).

Fig. 10 shows the distribution of the dissipated energy, W^p, in the 50-fib specimen of Fig. 1(b), subjected to a net pressure range of 320 MPa (see Fig. 2(c)). In such a case, plastic effects are distributed in a very small zone of only 0.001 mm (1/10 grain size) around the smaller notch (point A), where W^p assumes a maximum value of 6 MPa, evidencing elevated gradient effects. Plastic effects are also visible around the bigger notch (point B) where, however, W^p assumes a maximum value of about 0.5 MPa, comparable to the one obtained for the 50-notch specimen. The dissipated energy, W^p, is also plotted along the edge AB in Fig. 10.

The reported observations for the notch specimens are confirmed by the results of a linear elastic analysis conducted on each notched specimen to evaluate the stress concentration factor, K_t, defined as the ratio between the peak stress, σ_{peak}, at the root of the notch and the nominal stress, σ_{nom}, which would be present if a stress concentration did not occur [56]:

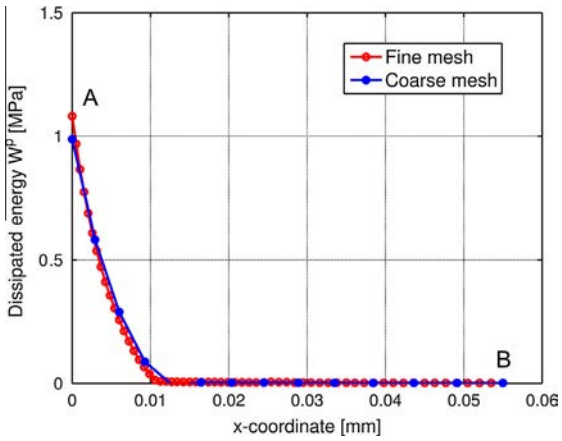

Fig. 9. Results of the mechanical analysis for the 50-notch specimen subjected to a net pressure range of 360 MPa. Comparison between two mesh refinements in terms of the dissipated energy, W^p, along the edge AB. The fine mesh has been used for the computations.

$$K_t = \frac{\sigma_{peak}}{\sigma_{nom}} \tag{6}$$

In particular, we obtain a value of approximately 2.4 for the 50-notch, 100-notch, and 145-notch specimens (in accordance with the values provided in [56]) and of 6 for the 50-fib specimen.

Fig. 11(a)–(b) shows the distribution of the dissipated energy, W^p in the 60-hole and 1500-slot specimens of Fig. 1(c)–(d), subjected to a net pressure range of 250 and 115 MPa, respectively (see Fig. 2(d)). The values assumed by the dissipated energy are higher for the 1500-slot specimen, notwithstanding the lower load, and additionally, are distributed in a very small zone. In this case, the stress concentration factor, K_t, assumes a value of approximately 3 for the 60-hole, 6 for the 400-slot, and 10 for the 1500-slot specimen.

In Fig. 12, the dissipated energy, W^p, is plotted along the edge AB of the 1500-slot specimen shown in Fig. 11(b), in order to highlight how mesh refinement does not allow noticeable improvements of the results in terms of dissipated energy also for the three-dimensional case. In particular, we show the results for the 1500-slot specimen which manifests high stress gradients.

However, in order to assure a coherence between the different computations, we recommend that all the meshes used for both the calibration of the constitutive law or fatigue criteria on the specimens and the structure should be refined in the critical areas with elements of comparable size. This technique permits to assure a coherence and a control of the error in all the cases (see also applications to welded structures in [57,58]). The remark with the constant mesh size applies also to Fig. 12, where we can note a difference in the area affected by the dissipation, i.e., plasticity, even if the hot-spot (point A) reaches more or less the same maximum.

4. 316L steel: fatigue analysis

This Section presents the second step of the adopted global computational approach, i.e., the fatigue analysis to compute the number of cycles before failure. Such an analysis is based on the investigation of the stabilized cycle obtained within the mechanical analysis described in Section 3.3. In particular, depending on the nature of the shakedown cycle, i.e., elastic or plastic, we use a Dang Van [34] or LCF crack initiation [37,38,10–12] criterion, respectively. All the criteria are calibrated on the described experimental campaigns in order to provide a set of criteria that can be used to numerically predict the fatigue-life of cardiovascular 316L stainless steel stents.

4.1. Elastic shakedown: Dang Van criterion

The classical Dang Van (DV) criterion [34] allows to define the limit of the imposed external load under which the structure will have an infinite life.

To this purpose, Dang Van considered the mesoscopic grain scale and the macroscopic structure scale, associated to the notion of representative volume element (RVE). The RVE has to contain a sufficient number of grains to be representative of average macroscopic mechanical properties, as in the present case. If the initial formulation of the DV criterion is not suitable to regions with inhomogeneous or high gradient stresses [47], its extension to welded structures [57,58] or analyses based on grain polycrystalline plasticity [41–44,30,46,47] permit to envision such an outcome which would be equally an entrance point to the VHCF regime.

The relations between mesoscopic and macroscopic fields can be reached, for example, using a homogenization scheme; see, e.g., [59,60]. In particular, by adopting the Lin–Taylor homogenization law, simple passages between the macroscopic and the mesoscopic scale (see, e.g., [61]) allow to state that the lifetime is infinite if the mesoscopic shear stress, $\tau_\mu(t)$, and the hydrostatic stress, $\sigma_h(t)$, satisfy the following inequality in all the points of the structure (subscript μ stands for mesoscopic variables):

$$\max_t \tau_\mu(t) + \alpha_\infty \sigma_h(t) \leqslant \beta_\infty \tag{7}$$

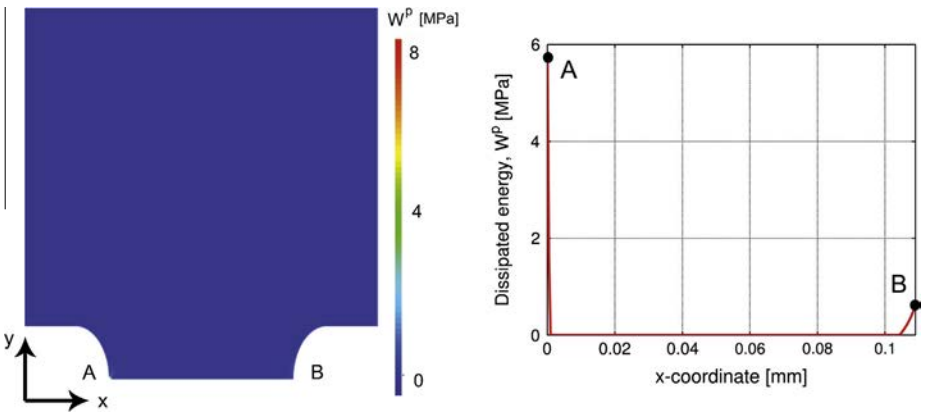

Fig. 10. Results of the mechanical analysis for the 50-fib subjected to a net pressure range of 320 MPa. Distribution of the dissipated energy, W^p, in the specimen (left) and along the edge AB (right).

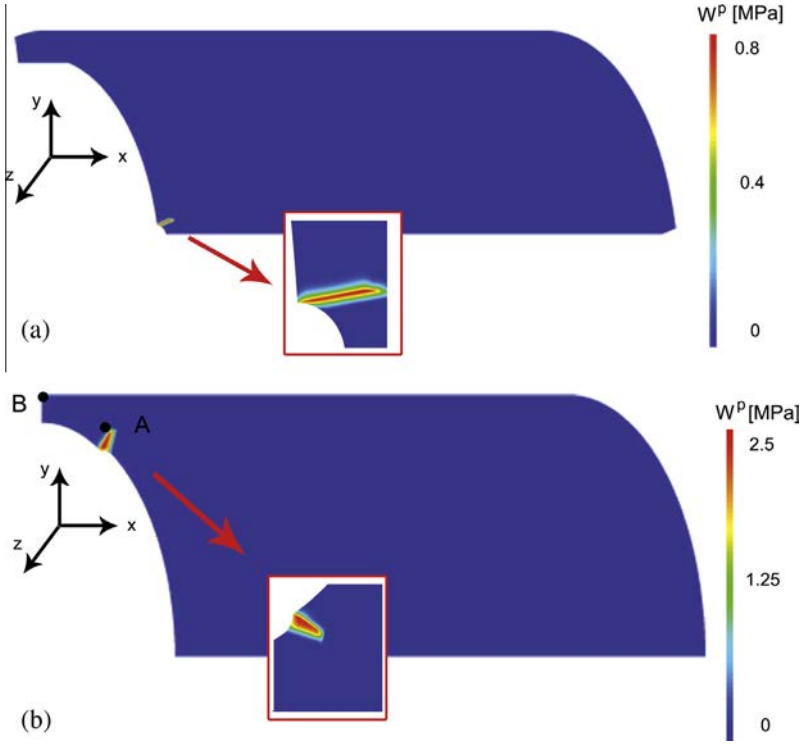

Fig. 11. Results of the mechanical analysis in terms of the dissipated energy, W^p, for the (a) 60-hole subjected to a net pressure range of 250 MPa; (b) 1500-slot subjected to a net pressure range of 115 MPa.

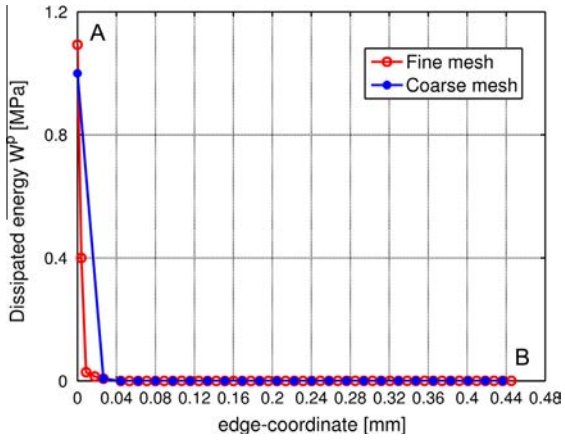

Fig. 12. Results of the mechanical analysis for the 1500-slot specimen subjected to a net pressure range of 115 MPa. Comparison between two mesh refinements in terms of the dissipated energy, W^p, along the edge AB. The fine mesh has been used for the computations.

where α_∞ and β_∞ are material parameters (subscript ∞ stands for infinite lifetime). Such parameters are usually deduced from two Wöhler curves related to smooth specimens, giving the fatigue limit in alternated torsion and fully reversed bending. In general, the Wöhler curves are not defined for an infinite number of cycles but rather for 10^6–10^7 cycles. Thus, in the following, we indicate these coefficients as α_N and β_N, where subscript N stands for finite lifetime [62–64].

Material parameters, α_N and β_N, can be also calibrated by considering two uniaxial cyclic loadings with respective ratios R_1 and R_2 and fatigue limits f_{R_1} and f_{R_2}. In the simple case of a cyclic uniaxial bending loading of R ratio, expressed in the classical form $\sigma_{xx}(t) = \sigma_a \sin \omega t + \sigma_m$, we derive the following equation:

$$\frac{\sigma_a}{2} + \alpha_N \frac{\sigma_a}{3}\left(1 + \frac{1+R}{1-R}\right) = \beta_N \quad \forall R \tag{8}$$

which can be generalized for two different loadings of ratios R_1 and R_2, as follows:

$$\frac{f_{R_i}}{2} + \alpha_N \frac{f_{R_i}}{3}\left(1 + \frac{1+R_i}{1-R_i}\right) = \beta_N \quad \text{for} \quad i = 1,2 \tag{9}$$

The following expressions for α_N and β_N are then obtained:

$$\begin{cases} \alpha_N = \frac{3}{4}\frac{f_{R_2} - f_{R_1}}{\frac{f_{R_1}}{1-R_1} - \frac{f_{R_2}}{1-R_2}} \\ \beta_N = \frac{f_{R_1} f_{R_2}}{\frac{f_{R_1}}{1-R_1} - \frac{f_{R_2}}{1-R_2}} \frac{R_1 - R_2}{2(1-R_1)(1-R_2)} \end{cases} \tag{10}$$

The DV parameters, α_N and β_N, are calibrated by using the experimental data on the smooth rectangular bars of 75, 100, and 150 μm widths, resulting in an elastic shakedown state (see Tables 4–6). The calibrated DV parameters refer to 10^7 cycles (i.e., $N = 10^7$) or to an equivalent stent implant period of approximately 8 months, instead of the requested 10^8 cycles [18]. We however remark that 10^7 cycles have already been considered as an infinite lifetime as, for example, in [65,66], coherently with the definition given in [25,23,26]. Although specimens tested by Wiersma et al. [23,25] and Donnelly [26] refer to a fatigue-life of 2×10^6 and 10^7 cycles, respectively, we could set $N = 10^7$ for the specimens used for the calibration, since the slope of the fatigue curves of

Table 9
DV parameters, α_N and β_N, referring to a fatigue-life, N, of 10^7 cycles and calibrated on data related to 75–150 μm and 50 μm width specimens [23,25,26], respectively.

Specimen width	Fatigue-life N	α_N	β_N
75–150 μm	10^7	0.4821	171.4286 MPa
50 μm	10^7	0.4821	137.1429 MPa

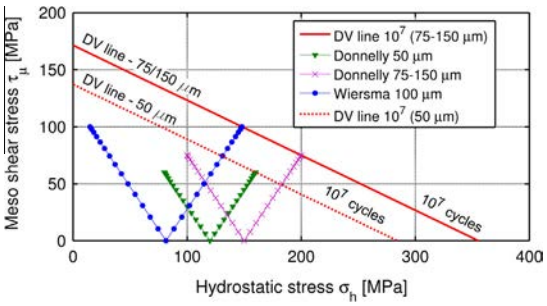

Fig. 13. DV lines in the hydrostatic-mesoscopic stress plane and loading paths from the tensile experiments used for calibration [25,23,26].

Fig. 2(b) is almost horizontal [23,25]. For safety reasons, we assume a reduced fatigue limit of 400 MPa for the specimens tested by Wiersma et al. [23,25] (see Table 4). Table 9 lists the DV parameters, calibrated on 75–150 µm width specimens.

Fig. 13 represents the diagram in terms of the mesoscopic shear stress, τ_μ, and the hydrostatic stress, σ_h, where the calibrated DV line (red smooth line) and the loading paths generated by the simulations of the experimental specimens of 75, 100, and 150 µm widths are represented. The maximum values for the hydrostatic stress are generated by the specimens tested by Donnelly [26] since presenting high values of mean stress, while the highest mesoscopic shear stresses are generated by the specimen tested by Wiersma et al. [23,25], presenting a higher load amplitude. Additionally, Fig. 13 shows the calibrated DV line (red dot line) related to the specimen of 50 µm width, which presents a lower value of the fatigue-life due to size effects [26]. As additional data for another R ratio is absent in this case, we construct such a DV line assuming the same slope as in the 75–150 µm width case. Table 9 also lists the DV parameters, calibrated on 50 µm width specimens.

4.2. Plastic shakedown: fatigue crack initiation criteria

A fatigue crack initiation criterion is classically defined as a local relation (i.e., in each spatial point of the structure, $x \in \Omega$), between the values of the mechanical fields, $(\boldsymbol{\varepsilon}, \boldsymbol{\varepsilon}^p, \boldsymbol{\sigma})$, computed for the stabilized cycle, and the number of cycles to failure, N_f, of the structure:

$$\max_{x\in\Omega}[f(\boldsymbol{\varepsilon}, \boldsymbol{\varepsilon}^p, \boldsymbol{\sigma})] = cN_f^b \tag{11}$$

where f represents the fatigue damage parameter that is characteristic of each criterion, while b and c are material parameters to be calibrated on experimental data.

In the present Section, we focus on the following criteria: (i) the Manson–Coffin criterion [35,36]; (ii) the dissipated energy per cycle criterion [37,38]; and (iii) a modified version of the dissipated energy criterion [10–12]. Moreover, in order to tackle the difficulties related to the high gradients of the fields close to the notched regions, we adopt a volumetric approach in the dissipated energy per cycle criterion. In the following, we present, first, the three criteria and then, we compare the obtained results.

4.2.1. Manson–Coffin fatigue criterion

The Manson–Coffin fatigue criterion is defined as follows [35,36]:

$$\Delta\epsilon^p = cN_f^b \tag{12}$$

where $f = \Delta\epsilon^p$ is the amplitude of the plastic strain in the uniaxial case. Since the considered experiments are multiaxial, we extend the amplitude, $\Delta\epsilon^p$, to this case as follows:

$$\Delta\epsilon^p = \max_{t_1}\max_{t_2}\sqrt{\frac{2}{3}[\epsilon^p(t_1)-\epsilon^p(t_2)] : [\epsilon^p(t_1)-\epsilon^p(t_2)]} \tag{13}$$

where t_1 and t_2 represent different time instants of the stabilized cycle. The present extension measures the diameter of the plastic strain path.

In the following, we denote the fatigue criterion as $\Phi_{\Delta\epsilon^p}$.

4.2.2. Dissipated energy per cycle criterion

The criterion based on the dissipated energy per cycle is defined as follows [37,38]:

$$W^p = cN_f^b \tag{14}$$

where $f = W^p$ is the dissipated energy per cycle, integrated in each point of the structure over the complete stabilized cycle, as follows:

$$W^p = \int_{cycle} \boldsymbol{\sigma} : \dot{\boldsymbol{\varepsilon}}^p dt \tag{15}$$

In the following, we denote the fatigue criterion as Φ_{W^p}.

4.2.3. Modified dissipated energy per cycle criterion

The definition of a fatigue parameter depending only on the dissipated energy implies that such a quantity is the only driving force of the damage, even if the effect of mean stress on fatigue is a well known phenomenon. Thus, we adopt the modified dissipated energy criterion proposed by Amiable et al. [10–12], as follows:

$$\left(W^p + a\sigma_h^{max}\right) = cN_f^b \tag{16}$$

where $f = \left(W^p + a\sigma_h^{max}\right)$ is the sum of the dissipated energy, W^p, and the maximal hydrostatic stress attended during the stabilized cycle, $\sigma_h^{max} = \max_t \sigma_h(t)$, with $\sigma_h = 1/3\mathrm{tr}(\boldsymbol{\sigma})$, while a is an additional material parameter.

In the following, the fatigue criterion is denoted as $\Phi_{W_{\sigma_h}}$.

4.2.4. Results and discussion

The identification of material parameters, a, b and c, is a regression problem which can be easily solved using existing solvers (e.g., the fitting tools, *cfootl* and *sftool*, in Matlab).

Such parameters are identified by postprocessing the values of the fatigue damage parameters, $\Delta\epsilon^p, W^p$, and $\left(W^p + a\sigma_h^{max}\right)$, computed at the root of the notch (hot-spot approach) or around the notch (volumetric approach).

Table 10
Calibrated material parameters, a, b, and c, and obtained correlation coefficient, R^2.

Criterion	Approach	a	b	c	R^2
$\Phi_{\Delta\epsilon^p}$	Hot-spot	–	−0.4214	0.6199	0.75
Φ_{W^p}	Hot-spot	–	−0.4687	431.4 MPa	0.74
Φ_{W^p}	Volume element – 0.005 mm	–	−0.5457	622.5 MPa	0.81
Φ_{W^p}	Volume element – 0.01 mm	–	−0.6187	907.8 MPa	0.86
Φ_{W^p}	Volume element – 0.02 mm	–	−0.6124	261.4 MPa	0.68
$\Phi_{W_{\sigma_h}}$	Hot-spot	0.00203	−0.3641	137.1 MPa	0.76

The volumetric approach considers a process volume for fatigue mechanisms [67,68] and assumes such a volume to be a cylinder for the three-dimensional specimens (slot and hole specimens) and a circle for the two-dimensional specimens (notch and fib specimens) with the center corresponding to the root of the notch. In three-dimensional structures, the cylinder is coherent with the spatial distribution of the mechanical fields. Moreover, its height is equal to the thickness of the slot and hole specimens, i.e., 90 μm. The optimal radius for both the cylinder and the circle is estimated as the minimizer of the statistical correlation coefficient, R^2, measuring the differences between the experimental and the predicted numbers of cycles to failure, as explained in the following.

The approach has been applied to the dissipated energy criterion, Φ_{W^p}. Averaging the dissipated energy inside a process volume is similar to the estimation of the distribution of plastic strain

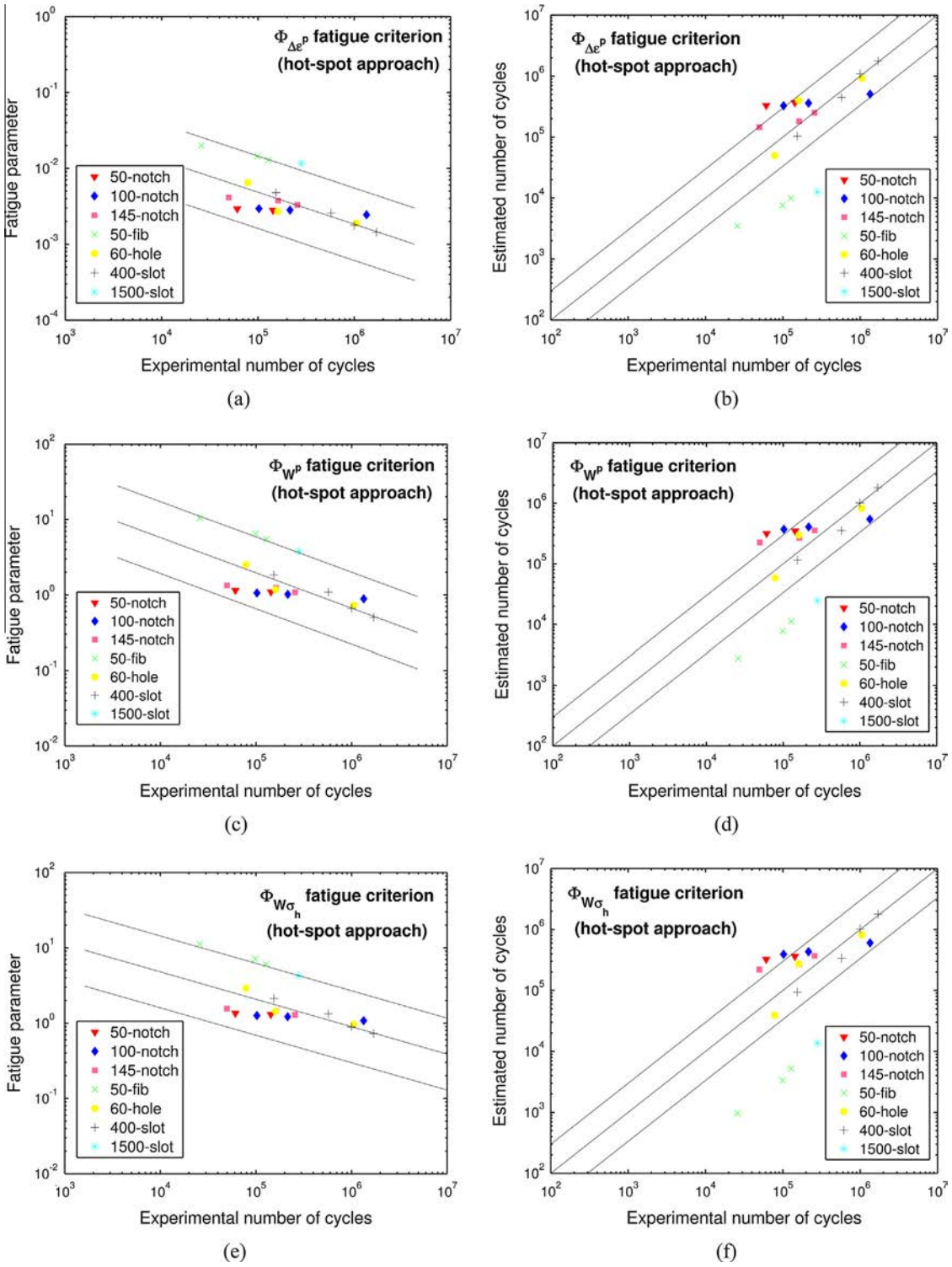

Fig. 14. Hot-spot approach for the $\Phi_{\Delta\varepsilon^p}$, Φ_{W^p}, and $\Phi_{W\sigma_h}$ fatigue criteria. (a)–(c)–(e) Fatigue parameter vs. experimental number of cycles to failure; (b)–(d)–(f) estimated vs. experimental number of cycles to failure.

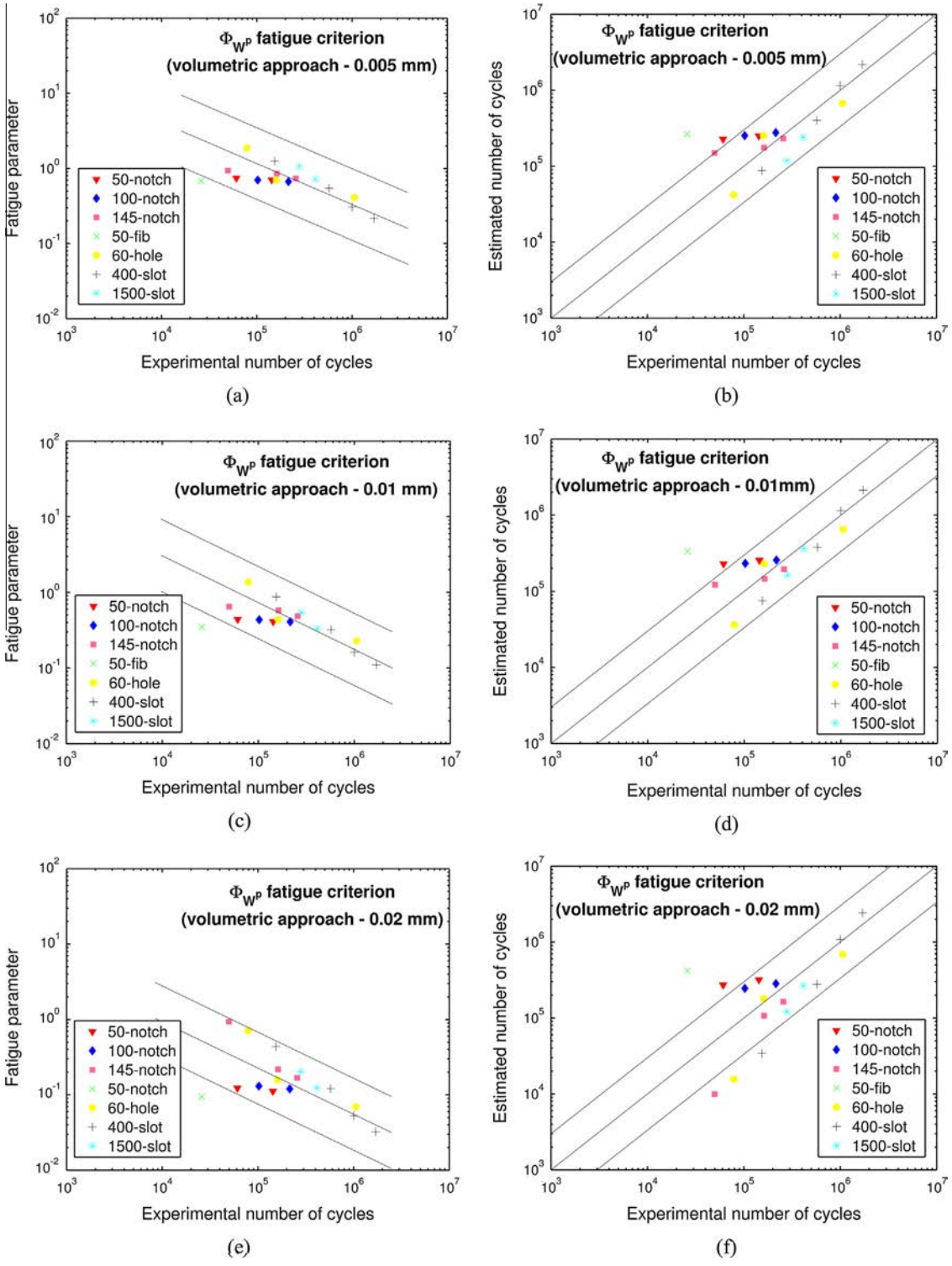

Fig. 15. Volumetric approach for the dissipated energy fatigue criterion, Φ_{W^p}. (a)–(c)–(d) Fatigue parameter vs. experimental number of cycles to failure; (b) estimated vs. experimental number of cycles to failure for volume-averaging radii of 0.005, 0.01, and 0.02 mm.

localized around the notch. The explored volumes have radii varying from 0.005 to 0.02 mm and the minimizer shows up to be 0.01 mm = 10 μm, which is actually the grain size of the material.

Table 10 lists the calibrated parameters, a, b and c, for the considered criteria. The values related to the volumetric approach are obtained for volume-averaging radii of 0.005, 0.01, and 0.02 mm. Figs. 14(a)–(c)–(e) and 15(a)–(c)–(e) present the diagram in terms of the fatigue parameter and the experimental number of cycles to failure, while Figs. 14(b)–(d)–(f) and 15(b)–(d)–(f) present the comparison between the experimental and the estimated number of cycles to failure for both the hot-spot and volumetric approaches. The results can be placed in a scattered band with a factor of ±3 on the number of cycles to failure, corresponding to the standard deviation.

As a first observation, the lifetimes predicted with the hot-spot approach are not well predicted by all the criteria, while the

volumetric approach related to the 0.01 mm radius gives very good results as the points are inside the ±3 factor on the lifetimes. The experimental number of cycles is often over-predicted with the hot-spot criteria. On the contrary, the hot-spot criteria predict safely lower numbers of cycles to failure for the 50-fib and 1500-slot specimens. As a consequence, one should consider the results obtained by the volumetric approach as a first estimation and then extend quantitatively the analysis in perspective, using one of the techniques proposed in [30,42–44] which explore the stress gradient effect and its interaction with crystal plasticity in a fatigue setting.

As it can be observed from Fig. 14(b)–(d)–(f), the hot-spot approach fails into predicting the fatigue limits of the 50-fib and 1500-slot specimens due to their high stress gradients and plastic strain localization at a distance of only few microns near the notch (see Section 3).

This aspect has been also treated by Wiersma et al. [25,23] who observed that the three notched bar specimens (i.e., the 50-notch, 100-notch, and 145-notch bars) have the same fatigue behavior in terms of net stress range (a fact which might be anticipated from basic notch theory, since the stress field of these notches is almost identical as well), as reported in Table 4. On the contrary, the fatigue limit of the 50-fib specimen is slightly lower. This has important consequences for the design of microscopic components, because it implies that very small root radii can be used in components such as stents, without compromising their fatigue behavior [23]. Slotted tube specimens (i.e., the 60-hole, 400-slot, and 1500-slot tubes) show a decreasing fatigue limit with increasing slot length (see Table 4).

Moreover, we observe that the dissipated energy criterion and its modified version present almost the same results. This can be due to the fact that both these criteria based on values computed at the root of the notch fail in case of high stress gradients. To this purpose, Fig. 16 presents the diagram in terms of the dissipated energy, W^p, and the maximal hydrostatic stress, σ_h^{max}, for all the specimens and shows very high values of the hydrostatic terms for the 50-fib and 1500-slot specimens. We observe also that there is a linear correlation between the dissipated energy and the maximal hydrostatic stress.

To compare accurately the prediction capabilities of the different criteria, we propose to use the correlation coefficient, R^2, corresponding to the linear association between experimental and computed fatigue lifetimes. R^2 is defined as in standard statistical textbooks [69], as follows:

$$R^2 = 1 - \frac{\sum_j \left(N_j^{exp} - N_j^{comp}\right)^2}{\sum_j \left(N_j^{exp} - \overline{N}\right)^2} \tag{17}$$

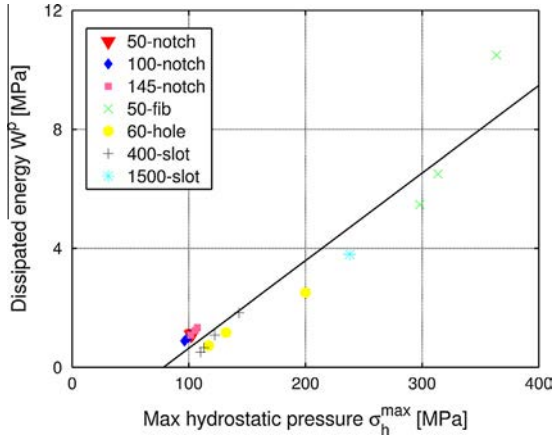

Fig. 16. Dissipated energy, W^p, vs. maximal hydrostatic stress, σ_h^{max}, computed at the root of the notch.

where N_j is the number of cycles related to experiment j (superscripts *exp* and *comp* stand for the experimental and the computed values of the number of cycles, respectively), and $\overline{N}$ is the mean of the experimental data.

Table 10 accounts the computed correlation coefficients for each criterion. The obtained values stretch in a reasonable range of reliability for the criteria (see, e.g., [70] for comparison). However, the results related to the hot-spot approach show relative low values of $R^2 \approx 0.74$–0.76, while the volumetric approach $R^2 = 0.86$ for the volume-averaging radius of 0.01 mm. As it can be observed, the radius of 0.01 mm gives the best correlation coefficient, compared to the 0.005 and 0.02 mm radii. Consequently, all the hot-spot approach criteria are relatively equivalent for the lifetime prediction, while the volumetric approach demonstrates its capability in lifetime prediction of notched μm-size specimens.

Although the selection of the averaging dimension is typically empirical, the proposed volumetric approach allows to give reasonable results in the prediction of crack initiation based on the stress and strain state of a volume of material.

5. Conclusions

The present paper has explored the fatigue of stainless steel components of μm-size by analyzing experimental data from the literature. The specimens were either smooth or notched and presented features similar to those characterizing cardiovascular stents. Our aim was to gain some insight in applications of 316L stainless steel for biomedical devices. These structures of very small sizes (of the order of grain size) are subjected to different environment conditions than standard applications as nuclear piping components. The present paper has investigated several fatigue criteria for infinite and finite lifetime, i.e., the fatigue criteria by Dang Van and Manson–Coffin as well as the dissipated energy per cycle criterion and its modified version, associated with hot-spot as well as volume element approaches. The results have demonstrated that the volume element approach is efficient in the presence of high stress gradients and size effects. The provided criteria, calibrated on suitable experimental data, can be used in the numerical fatigue-life assessment of cardiovascular 316L stainless steel stents. We remark, however, that the proposed approach ignores the inhomogeneous nature of the microstructure.

In order to effectively demonstrate the reliability of the calibrated fatigue criteria and their application to stent design, an ongoing work will propose a computational approach for the fatigue-life assessment of balloon-expandable stents, which combines advanced numerical methods with lifetime prediction methodologies and available material fatigue data. The main idea is to obtain a reliable, general and coherent fatigue prediction methodology through the application of a global computational approach composed of a mechanical finite element analysis, followed by a fatigue analysis. The fatigue analysis will be conducted by applying the proposed criteria depending on the obtained stabilized cycle of the investigated stent.

Moreover, the idea of introducing the material variability as a probability density function will be the object of future work.

Acknowledgement

This work is partially funded by Ministero dell'Istruzione, dell'Università e della Ricerca through the Project No. 2010BFXRHS and by the Italian-French University (UIF-UIF) through the 'Bando Galileo 2013–2014' Grant No. 148-30174*TJ*.

References

[1] Baddoo N. Stainless steel in construction: a review of research, applications, challenges and opportunities. J Constr Steel Res 2008;64:1199–206.
[2] Polak J, Obrtlik K, Hajek M. Cyclic plasticity in type 316L austenitic stainless steel. Fatigue Fract Eng Mater Struct 1994;17:773–82.
[3] Pham M, Solenthaler C, Janssens K, Holdsworth S. Dislocation structure evolution and its effects on cyclic deformation response of AISI 316L stainless steel. Mater Sci Eng A 2011;528(7-8):3261–9.
[4] Gerland M, Violan P. Secondary cyclic hardening and dislocation structures in type 316 stainless steel at 600C. Mater. Sci. Eng. 1986;84(0):23–33.
[5] Alain R, Violan P, Mendez J. Low cycle fatigue behavior in vacuum of a 316L type austenitic stainless steel between 20 and 600C. Part I: fatigue resistance and cyclic behavior. Mater Sci Eng A 1997;229:87–94.
[6] Lemaitre J, Chaboche J. Mechanics of solid materials. Cambridge University Press; 1994.
[7] Huang J, Yeh J, Jeng S-L, Chen C, Kuo R. High-cycle fatigue behavior of type 316L stainless steel. Mat Trans 2006;47:409–17.
[8] Puchi-Cabrera E, Staia M, Tovar C, Ochoa-Pérez E. High cycle fatigue behavior of 316L stainless steel. Int J Fatigue 2008;30(12):2140–6.
[9] Mohammad K, Zainudin E, Salit M, Zahari N, Ali A. Experimental determination of the fatigue behavior of austenitic 316L stainless steel under fatigue and creep-fatigue tests at high temperature. Int J Metal Steel Res Tech 2013;1(1):1–11.
[10] Amiable S, Chapuliot S, Constantinescu A, Fissolo A. A comparison of lifetime prediction methods for a thermal fatigue experiment. Int J Fatigue 2006;28(7):692–706.
[11] Amiable S, Chapuliot S, Constantinescu A, Fissolo A. A computational lifetime prediction for a thermal shock experiment. Part I: thermomechanical modeling and lifetime prediction. Fatigue Fract Eng Mater Struct 2009;29: 209–17.
[12] Amiable S, Chapuliot S, Constantinescu A, Fissolo A. A computational lifetime prediction for a thermal shock experiment. part II: discussion on different fatigue criteria. Fatigue Fract Eng Mater Struct 2009;29:219–27.
[13] Le Pécheur A, Curtit F, Clavel M, Stephan J, Rey C, Bompard P. Thermo-mechanical FE model with memory effect for 304L austenitic stainless steel presenting microstructure gradient. Int J Fatigue 2012;45:106–15.
[14] Laamouri A, Sidhom H, Braham C. Evaluation of residual stress relaxation and its effect on fatigue strength of AISI 316L stainless steel ground surfaces: Experimental and numerical approaches. Int J Fatigue 2013;48:109–21.
[15] Winters G, Nutt M. Stainless steel for medical and surgical applications. In: ASMT International; 2003.
[16] Bombac D, Brojan M, Fajfar P, Kosel F, Turk R. Review of materials in medical applications. Mater Geoenv 2007;54:471–99.
[17] Dumoulin C, Cochelin B. Mechanical behaviour of balloon expandable stents. J Biomech 2000;33:1461–70.
[18] Food U, Administration D. Non-clinical engineering tests and recommended labeling for intravascular stents and associated delivery systems: guidance for industry and FDA staff. In: US department of health and human services; food and drug administration, centre for devices and radiological, health (18.04.10).
[19] Harewood F, McHugh P. Modeling of size dependent failure in cardiovascular stent struts under tension and bending. Ann Biomed Eng 2007;35(9):1539–53.
[20] Murphy B, Savage P, McHugh P, Quinn D. The stressstrain behavior of coronary stent struts is size dependent. Ann Biomed Eng 2003;31:686–91.
[21] Murphy B, Cuddy H, Harewood F, Connolley T, McHugh P. The influence of grain size on the ductility of micro-scale stainless steel stent struts. J Mater Sci: Mater Med 2006;17(1):1–6.
[22] You X, Connolley T, Mchugh P, Cuddy H, Motz C. A combined experimental and computational study of deformation in grains of biomedical grade 316LVM stainless steel. Acta Mater 2006;54:4825–40.
[23] Wiersma S, Dolan F, Taylor D. Fatigue and fracture in materials used for micro-scale biomedical components. Bio-med Mater Eng 2006;16(2):137–46.
[24] Connolley T, McHugh PE, Bruzzi M. A review of deformation and fatigue of metals at small size scales. Fatigue Fract Eng Mater Struct 2005;28(12): 1119–52.
[25] Wiersma S, Taylor D. Fatigue of materials used in microscopic components. Fatigue Fract Eng Mater Struct 2005;28(12):1153–60.
[26] Donnelly E. Geometry effect in the fatigue behaviour of microscale 316L stainless steel specimens, Ph.D. thesis, National University of Ireland, Galway; 2012.
[27] dos Santos H, Auricchio F, Conti M. Fatigue life assessment of cardiovascular balloon-expandable stents: a two-scale plasticity-damage model approach. J Mech Behav Biomed 2012;15:78–92.
[28] Barrera O, Makradi A, Abbadi M, Azaouzi M, Belouettar S. On high-cycle fatigue of 316L stents. Comput Methods Biomech Biomed Eng 2012;0:1–12.
[29] McGarry J, Ø'Donnell B, McHugh P, McGarry J. Analysis of the mechanical performance of a cardiovascular stent design based on micromechanical modelling. Comput Mater Sci 2004;31:421–38.
[30] Sweeney C, McHugh P, McGarry J, Leen S. Micromechanical methodology for fatigue in cardiovascular stents. Int J Fatigue 2012;44:202–16.
[31] Azaouzi M, Makradi A, Belouettar S. Fatigue life prediction of cardiovascular stent using finite element method. Comput Methods Biomech Biomed Eng 2012;15(S1):93–5.
[32] Auricchio F, Di Loreto M, Sacco E. Finite-element analysis of a stenotic artery revascularization through a stent insertion. Comput Methods Biomech Biomed Eng 2001;4(3):249–63.
[33] Constantinescu A, Dang Van K, Charkaluk E. A unified approach for high and low cycle fatigue based on shakedown concepts. Fatigue Fract Eng Mater Struct 2003;26:561–8.
[34] Dang-Van K. High-cycle metal fatigue in the context of mechanical design. In: Van K, Papadopoulos I, editors. CISM courses and lectures, vol. 392. Springer-Verlag; 1999. p. 57–88.
[35] Manson S, Behaviour of materials under conditions of thermal stresses. Tech. rep., N.A.C.A., TN 2933; 1953.
[36] Coffin L. A study of the effects of cyclic thermal stresses on a ductile metal. Trans ASME 1953;53-A76:931–50.
[37] Korsunsky A, Dini D, Dunne F, Walsh M. Comparative assessment of dissipated energy and other fatigue criteria. Int J Fatigue 2007;29(9-11):1990–5.
[38] Charkaluk E, Constantinescu A. Dissipative aspects in high cycle fatigue. Mech Mater 2009;41(5):483–94.
[39] Grogan J, Leen S, McHugh P. Influence of statistical size effects on the plastic deformation of coronary stents. J Mech Behav Biomed 2013;20:61–76.
[40] McGarry J, Ø'Donnell B, McMeeking R, McHugh P, Ø'Cearbhaill E. Computational examination of the effect of material inhomogeneity on the necking of stent struts under tensile loading. J Appl Mech 2007;74(5):978–89.
[41] Hofmann F, Bertolino G, Constantinescu A, Ferjani M. Numerical exploration of the Dang Van high cycle fatigue criterion: application to gradient effects. J Mech Mater Struct 2009;4(2):293–308.
[42] Bertolino G, Constantinescu A, Ferjani M, Treiber P. A multiscale approach of fatigue and shakedown for notched structures. Theor Appl Fract Mech 2007;48(2):140–51.
[43] Guerchais R, Robert C, Morel F, Saintier N. Micromechanical study of the loading path effect in high cycle fatigue. Int J Fatigue 2014;59(0):64–75.
[44] Guerchais R, Saintier N, Morel F, Robert C. Micromechanical investigation of the influence of defects in high cycle fatigue. Int J Fatigue 2014;x(0). xx–xx. doi:http://dx.doi.org/10.1016/j.ijfatigue.2014.01.005.
[45] McDowell D, Dunne F. Microstructure-sensitive computational modeling of fatigue crack formation. Int J Fatigue 2010;32(9):1521–42.
[46] Sweeney C, Vorster W, Leen S, Sakurada E, McHugh P, Dunne F. The role of elastic anisotropy, length scale and crystallographic slip in fatigue crack nucleation. J Mech Phys Solids 2013;61:1224–40.
[47] Sweeney C, O'Brien B, McHugh P, Leen S. Experimental characterisation for micromechanical modelling of CoCr stent fatigue. Biomaterials 2014;35:36–48.
[48] Lê M-B. Propagation de fissure par fatigue en présence d'une pré-déformation et de contraintes résiduelles, Ph.D. thesis, École Polytechnique; 2013.
[49] Cast3M, Documentation Cast3M; 2013. <http://www-cast3m.cea.fr>.
[50] Skelton R. Energy criterion for high temperature low cycle fatigue failure. Mater Sci Tech SER 1991;7:427–39.
[51] Skelton R. Cyclic hardening, softening, and crack growth during high temperature fatigue. Mater Sci Tech SER 1993;9:1001–8.
[52] Morhácová E. Relation between monte carlo simulations of grain growth and real structures. Crystal Res Technol 1995;30(1):K9–K12.
[53] Benallal A, Marquis D. Constitutive equations for nonproportional cyclic elastoviscoplasticity. J Eng Mater – T ASME 1987;109:326–36.
[54] Krempl E, Khan F. Rate (time)-dependant deformation behavior: an overview of some properties of metal and solid polymers. Int J Plasticity 2003;19:1069–95.
[55] Chaboche J, Dang Van K, Cordier K. Modelisation of the strain memory effect on the cycle hardening of 316L stainless steel. In: Proceedings SMIRT 5, vol. M; 1979.
[56] Pilkey W, Pilkey D. Petersoń s stress concentration factors. John Wiley & Sons Inc.; 2008.
[57] Fayard J, Bignonnet A, Van K. Fatigue design criterion formability welded structures. Fatigue Fract Eng Mater Struct 1996;19(6):723–9.
[58] Dang Van K, Bignonnet A, Fayard JL, Janosch JJ. Assessment of welded structures by a local multiaxial fatigue approach. Fatigue Fract Eng Mater Struct 2001;24(5):369–76.
[59] Cano F, Constantinescu A, Maitournam H. Critere de fatigue polycyclique pour des materiaux anisotropes: application aux monocristaux. CR Mecanique 2004;332(2):115–21.
[60] Monchiet V, Charkaluk E, Kondo D. A plasticity-damage based micromechanical modelling in high cycle fatigue. CR Mecanique 2006;334(2):129–36.
[61] Dang Van K, Griveau B, Message O. On a new multiaxial fatigue limit criterion: theory and application. In: Brown M, Miller K, editors. Biaxial and multiaxial fatigue (EGF 3). London: Mechanical Engineering Publications; 1989. p. 479–96.
[62] Ferjani M, Averbuch D, Constantinescu A. Semianalytical solution for the stress distribution in notched tubes. Int J Fatigue 2011;33(4):557–67.
[63] Ferjani M, Averbuch D, Constantinescu A. A computational approach for the fatigue design of threaded connections. Int J Fatigue 2011;33:610–23.
[64] Wackers P, Alquezar-Getan M, Constantinescu A, Maitournam H, Arrieta V. A modeling approach to predict fretting fatigue on highly loaded blade roots. J Eng Gas Turbines Power 2010;132(8):1–9.
[65] Subash S. Fatigue of materials. Cambridge University Press; 1998.
[66] Pelton A, Schroeder V, Mitchell M, Gong X-Y, Barney M, Robertson S. Fatigue and durability of Nitinol stents. J Mech Behav Biomed 2008;1:153–64.

[67] Maitournam M, Dang Van K, Flavenot J. Fatigue design of notched components with stress gradients and cyclic plasticity. Adv Eng Mater 2009;11(9):750–4.
[68] Dang Van K, Maitournan H, Flavenot J. Fatigue design of notched components by a multiscale approach based on shakedown. In: Pluvinage G, Sedmak A, editors. Security and reliability of damaged structures and defective materials. NATO science for peace and security series c: environmental security. Netherlands: Springer; 2009. p. 325–36.
[69] Di Bucchianico A. Coefficient of determination (R2). John Wiley & Sons, Ltd.; 2008.
[70] Tabibian S, Charkaluk E, Constantinescu A, Szmytka F, Oudin A. TMF-LCF life assessment of a Lost Foam Casting A319 aluminum alloy. Int J Fatigue 2013;53(0):75–81.